

The public reporting burden for this collection of information is estimated to average 1 hour per response, including the time for reviewing instructions, searching existing data sources, gathering and maintaining the data needed, and completing and reviewing the collection of information. Send comments regarding this burden estimate or any other aspect of this collection of information, including suggestions for reducing this burden, to Washington Headquarters Services, Directorate for Information Operations and Reports, 1215 Jefferson Davis Highway, Suite 1204, Arlington VA, 22202-4302. Respondents should be aware that notwithstanding any other provision of law, no person shall be subject to any penalty for failing to comply with a collection of information if it does not display a currently valid OMB control number.  
PLEASE DO NOT RETURN YOUR FORM TO THE ABOVE ADDRESS.

1. REPORT DATE (DD-MM-YYYY) 31-01-2014	2. REPORT TYPE Final Report	3. DATES COVERED (From - To) 1-Apr-2013 - 31-Dec-2013
---	--------------------------------	--

4. TITLE AND SUBTITLE Active Flow Control with Thermoacoustic Actuators	5a. CONTRACT NUMBER W911NF-13-1-0062
	5b. GRANT NUMBER
	5c. PROGRAM ELEMENT NUMBER 611102

6. AUTHORS Kunihiko Taira	5d. PROJECT NUMBER
	5e. TASK NUMBER
	5f. WORK UNIT NUMBER

7. PERFORMING ORGANIZATION NAMES AND ADDRESSES Florida State University Sponsored Research Services 874 Traditions Way Tallahassee, FL 32306 -4166	8. PERFORMING ORGANIZATION REPORT NUMBER
--	--

9. SPONSORING/MONITORING AGENCY NAME(S) AND ADDRESS (ES) U.S. Army Research Office P.O. Box 12211 Research Triangle Park, NC 27709-2211	10. SPONSOR/MONITOR'S ACRONYM(S) ARO
	11. SPONSOR/MONITOR'S REPORT NUMBER(S) 63843-EG-II.1

12. DISTRIBUTION AVAILABILITY STATEMENT Approved for Public Release; Distribution Unlimited
--

13. SUPPLEMENTARY NOTES The views, opinions and/or findings contained in this report are those of the author(s) and should not be construed as an official Department of the Army position, policy or decision, unless so designated by other documentation.
---

14. ABSTRACT We numerically examine the effectiveness of thermoacoustic actuators that locally introduce high-intensity acoustic waves for active flow control. In this investigation, we perform LES of flow control with acoustic waves motivated by the recent development in manufacturing graphene/carbon nanotube-based surface compliant loud speakers. The interaction of the acoustic waves and turbulent flow structures is analyzed with high-fidelity LES for compressible flow over a wall-mounted hump at a Reynolds number of $0.5 \times 10^6$ and Mach number of 0.25. In the computations, we consider the use of high-frequency excitation at Helmholtz number of 2 based on performance
--

15. SUBJECT TERMS flow control, acoustics, large-eddy simulation
---

16. SECURITY CLASSIFICATION OF:	17. LIMITATION OF ABSTRACT	15. NUMBER OF PAGES	19a. NAME OF RESPONSIBLE PERSON
a. REPORT UU	UU		Kunihiko Taira
b. ABSTRACT UU			19b. TELEPHONE NUMBER 850-645-0140
c. THIS PAGE UU			

## Report Title

Active Flow Control with Thermoacoustic Actuators

### ABSTRACT

We numerically examine the effectiveness of thermoacoustic actuators that locally introduce high-intensity acoustic waves for active flow control. In this investigation, we perform LES of flow control with acoustic waves motivated by the recent development in manufacturing graphene/carbon nanotube-based surface compliant loud speakers. The interaction of the acoustic waves and turbulent flow structures is analyzed with high-fidelity LES for compressible flow over a wall-mounted hump at a Reynolds number of  $0.5 \times 10^6$  and Mach number of 0.25. In the computations, we consider the use of high-frequency actuation at Helmholtz number of 3 based on performance characteristics of the graphene-based thermoacoustic actuators. We observe that the actuation is able to introduce small-scale perturbation to the shear layer in the separated flow and delay the formation of large-scale spanwise vortices. This hence elongates the recirculation zone and shifts the low-pressure region downstream of the hump. As a consequence, the drag on the hump is reduced by approximately 5% for the three-dimensional calculation and up to 10% in the two-dimensional flow. The mechanism of drag reduction is different from the one using synthetic jets, which relies on reducing the size of the recirculation zone.

---

**Enter List of papers submitted or published that acknowledge ARO support from the start of the project to the date of this printing. List the papers, including journal references, in the following categories:**

**(a) Papers published in peer-reviewed journals (N/A for none)**

<u>Received</u>	<u>Paper</u>
-----------------	--------------

**TOTAL:**

**Number of Papers published in peer-reviewed journals:**

---

**(b) Papers published in non-peer-reviewed journals (N/A for none)**

<u>Received</u>	<u>Paper</u>
-----------------	--------------

**TOTAL:**

**Number of Papers published in non peer-reviewed journals:**

---

**(c) Presentations**

Number of Presentations: 0.00

---

**Non Peer-Reviewed Conference Proceeding publications (other than abstracts):**

Received      Paper

**TOTAL:**

Number of Non Peer-Reviewed Conference Proceeding publications (other than abstracts):

---

**Peer-Reviewed Conference Proceeding publications (other than abstracts):**

Received      Paper

**TOTAL:**

Number of Peer-Reviewed Conference Proceeding publications (other than abstracts):

---

**(d) Manuscripts**

Received      Paper

**TOTAL:**

Number of Manuscripts:

---

**Books**

Received      Paper

**TOTAL:**

## Patents Submitted

---

## Patents Awarded

---

## Awards

---

## Graduate Students

<u>NAME</u>	<u>PERCENT SUPPORTED</u>	Discipline
Jantzen, Ryan	0.11	
Munday, Phillip	0.70	
Yeh, Chi An	0.52	
<b>FTE Equivalent:</b>	<b>1.33</b>	
<b>Total Number:</b>	<b>3</b>	

## Names of Post Doctorates

<u>NAME</u>	<u>PERCENT SUPPORTED</u>
Bin, JongHoon	0.34
<b>FTE Equivalent:</b>	<b>0.34</b>
<b>Total Number:</b>	<b>1</b>

## Names of Faculty Supported

<u>NAME</u>	<u>PERCENT SUPPORTED</u>	National Academy Member
Kunihiko Taira	0.00	
William Oates	0.00	
<b>FTE Equivalent:</b>	<b>0.00</b>	
<b>Total Number:</b>	<b>2</b>	

## Names of Under Graduate students supported

<u>NAME</u>	<u>PERCENT SUPPORTED</u>
<b>FTE Equivalent:</b>	
<b>Total Number:</b>	

### Student Metrics

This section only applies to graduating undergraduates supported by this agreement in this reporting period

The number of undergraduates funded by this agreement who graduated during this period: ..... 0.00

The number of undergraduates funded by this agreement who graduated during this period with a degree in science, mathematics, engineering, or technology fields:..... 0.00

The number of undergraduates funded by your agreement who graduated during this period and will continue to pursue a graduate or Ph.D. degree in science, mathematics, engineering, or technology fields:..... 0.00

Number of graduating undergraduates who achieved a 3.5 GPA to 4.0 (4.0 max scale):..... 0.00

Number of graduating undergraduates funded by a DoD funded Center of Excellence grant for Education, Research and Engineering:..... 0.00

The number of undergraduates funded by your agreement who graduated during this period and intend to work for the Department of Defense ..... 0.00

The number of undergraduates funded by your agreement who graduated during this period and will receive scholarships or fellowships for further studies in science, mathematics, engineering or technology fields: ..... 0.00

### Names of Personnel receiving masters degrees

NAME

**Total Number:**

### Names of personnel receiving PHDs

NAME

**Total Number:**

### Names of other research staff

NAME

PERCENT SUPPORTED

**FTE Equivalent:**

**Total Number:**

### Sub Contractors (DD882)

### Inventions (DD882)

### Scientific Progress

(1) Conducted large-eddy simulations (LES) of three-dimensional turbulent flow over a wall-mounted hump (NASA validation workshop problem) at  $Re_{\infty} = 0.5 \times 10^6$  and  $M_{\infty} = 0.25$  and validated the results with other experimental and computational studies. This computational setup serves as a numerical testbed for various flow control parameter studies.

(2) Formulated a thermoacoustic actuator wall model that be used in LES or DNS to predict actuator performance in flow control applications.

(3) Performed two and three-dimensional flow control simulations with thermoacoustic actuation modeled through a wall boundary condition. Modification of the turbulent flow field and reduction in drag on the hump are observed.

(4) Analyzed the interaction between the turbulent separated flow and acoustic waves responsible for modifying the wake downstream of the hump.

# Technology Transfer

# Final Report

## STIR: Active Flow Control with Thermoacoustic Actuators

ARO Grant W911NF-13-1-0062  
(April 1, 2013–December 13, 2013)

PI: Kunihiko Taira  
*Department of Mechanical Engineering*  
*Florida A&M/Florida State University, Tallahassee, FL 32310*

### Abstract

We numerically examine the effectiveness of thermoacoustic actuators that locally introduce high-intensity acoustic waves for active flow control. The use of near-field acoustic excitation in flow control applications has not been explored deeply in the past due to the absence of surface-compliant actuators that are capable of delivering high-intensity acoustic waves. In this investigation, we perform LES of flow control with acoustic waves motivated by the recent development in manufacturing graphene/carbon nanotube-based surface compliant loud speakers. The interaction of the acoustic waves and turbulent flow structures is analyzed with high-fidelity LES for compressible flow over a wall-mounted hump at a Reynolds number of  $0.5 \times 10^6$  and Mach number of 0.25. In the computations, we consider the use of high-frequency actuation at Helmholtz number of 3 based on performance characteristics of the graphene-based thermoacoustic actuators. We observe that the actuation is able to introduce small-scale perturbation to the shear layer in the separated flow and delay the formation of large-scale spanwise vortices. This hence elongates the recirculation zone and shifts the low-pressure region downstream of the hump. As a consequence, the drag on the hump is reduced by approximately 5% for the three-dimensional calculation and up to 10% in the two-dimensional flow. The mechanism of drag reduction is different from the one using synthetic jets, which relies on reducing the size of the recirculation zone.

## Contents

<b>1</b>	<b>Major Accomplishments</b>	<b>3</b>
<b>2</b>	<b>Introduction</b>	<b>3</b>
<b>3</b>	<b>Computational Approach</b>	<b>5</b>
3.1	Validation . . . . .	6
<b>4</b>	<b>Thermoacoustic Actuator Model</b>	<b>9</b>
<b>5</b>	<b>Active Flow Control with Acoustic Waves</b>	<b>10</b>
5.1	Two-Dimensional Flow . . . . .	11
5.2	Three-Dimensional Flow . . . . .	14
<b>6</b>	<b>Summary</b>	<b>19</b>
<b>7</b>	<b>Personnel</b>	<b>21</b>

# 1 Major Accomplishments

1. Conducted large-eddy simulations (LES) of three-dimensional turbulent flow over a wall-mounted hump (NASA validation workshop problem) at  $Re_\infty = 0.5 \times 10^6$  and  $M_\infty = 0.25$  and validated the results with other experimental and computational studies. This computational setup serves as a numerical test bed for various flow control parameter studies.
2. Formulated a thermoacoustic actuator wall model that be used in LES or DNS to predict actuator performance in flow control applications.
3. Performed two and three-dimensional flow control simulations with thermoacoustic actuation modeled through a wall boundary condition. Modification of the turbulent flow field and reduction in drag on the hump are observed.
4. Analyzed the interaction between the turbulent separated flow and acoustic waves responsible for modifying the wake downstream of the hump.

# 2 Introduction

Active flow control has been applied to various aerodynamic systems for performance enhancement, such as lift increase, drag reduction and, mixing enhancement [1]. The main challenge of active flow control is to determine how and where one can introduce the control input to modify the flow field favorably with minimal energy input. In past applications, active flow control has been performed by injecting mass, momentum, or vorticity (or the combination thereof) in either a steady or unsteady fashion using various types of devices [2], such as the synthetic jets [3], dielectric barrier discharge (DBD) plasma actuators [4], or combustion powered actuators [5]. Compared to passive flow control techniques, such as vortex generators, the use of active flow control has not been widespread for general aerodynamic enhancements (despite the adaptive capability of active flow control). There are two main factors for restricting the implementation of active flow control. First is the bulkiness due to the weight and size of the actuator device which limits the location it can be embedded. Second is the amount of power required to deliver the control perturbation into the flow field, which is fairly large because of the limited device efficiency.

To address the above two limitations, we consider the use of a novel speaker made of carbon nanotubes/graphene as a flow control actuator. A membrane of carbon nanotubes/graphene laid on a backing material such as paper under AC power has been shown to produce large-amplitude acoustic waves [6]. The input AC current sinusoidally heats this device due to joule heating and creates surface pressure disturbances that are emitted as acoustic waves to the surrounding fluid [7, 8]. One of the attractive characteristics of this carbon-based sound-emitting device is its sheet-like arrangement that can be applied to essentially any surface, without occupying any internal space nor adding significant weight, which is similar to how DBD plasma actuators can be installed.

The sound generation mechanism, known as thermophone, was discovered with platinum much earlier (1917) [9] but has not been widely utilized due to the relatively large power required. Compared to conventional metals, the heat capacity value for carbon-based material (carbon nanotubes/graphene) in consideration here is at least 2 orders of magnitude smaller. Since the output acoustic power delivered to the surrounding flow field is related inversely to the material heat capacity  $C$  (i.e.,  $P_{\text{output}} \propto C^{-1}P_{\text{input}}$ ), the use of carbon-based material dramatically enhances the device efficiency. According to the measurements reported in Tian et al. [6] and Lin et al. [10], the carbon-based devices are able to deliver constant noise levels of  $\approx 85\text{dB}$  over a broad range of frequency, 10-50 kHz, which should be of interest for many flow control applications [11].

Past studies have shown that inherent acoustic feedback mechanisms in flow over a cavity [12] or impinging jet [13] yield significantly different flow behavior compared to cases without the presence of such feedback path. There are also reports of acoustic perturbation being able to modify the flow over airfoils [14] or stabilize combustion instabilities [15] from external acoustic input (not attached to the body surface). We however re-emphasize that past acoustic actuators could not be readily mounted on the surface of bodies due to their size (including synthetic jets that relies mostly on momentum injection). The present study will examine how strong acoustic perturbation introduced locally can alter the flow field based on a surface-mounted thermoacoustic actuator.

The objective of the present study is to gain insights into how thermoacoustic actuators based on carbon nanotubes/graphene can alter turbulent separated flows. A boundary condition model [16] that captures the generation of thermoacoustic waves is implemented in the LES for flow over a wall-mounted hump to examine the influence of thermoacoustic perturbation on reducing drag and shortening the recirculation bubble. The hump geometry is chosen from the NASA Validation Workshop [17, 18, 19, 20], shown in Figure 1. The use of this hump geometry facilitates the assessment of the thermoacoustic actuator performance against other types of actuators. This specific problem is chosen to assess the performance of high-intensity acoustic waves for turbulent flow modification. The Reynolds number and Mach numbers are chosen to be  $Re = 0.5 \times 10^6$  and  $M_\infty = 0.25$ , respectively.

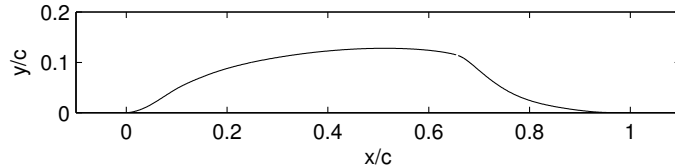


**Figure 1:** Geometry of the NASA workshop hump model.

Below we describe computational approach taken in this study and present the validation cases in Section 3. We then describe the thermoacoustic actuator in Section 4. Flow control findings from the performed LES for two and three-dimensional flow are presented. It is found that the thermoacoustic actuator can alter the turbulent flow field and achieve drag reduction on the wall-mounted hump in Section 5. At last in Section 6, we provide a summary of the present study and comments on possible future tasks to further understand

the mechanism of active flow control using locally added high-intensity acoustic waves.

### 3 Computational Approach

Numerical simulations of flow over the wall-mounted hump are performed with CharLES [21, 22, 23] to accurately predict the turbulent flow field as well as the acoustic field. The accuracy of the compressible flow solver CharLES is formally second order in space and third order in time. The flow over the hump is examined using LES with the Vreman model, since the small-scale vortical structures generated at the considered Reynolds number can be smaller than the grid resolution near the wall. The Reynolds number and Mach number of  $Re \equiv \rho_\infty U_\infty c / \mu_\infty = 0.5 \times 10^6$  and  $M_\infty \equiv U_\infty / a_\infty = 0.25$  are chosen to match representative cases considered in the NASA Validation Workshop [18, 19, 20].

The computational domain size is chosen to match the experimental setup given by the workshop guidelines [17] and the study conducted by Greenblatt *et al.* [24]. The streamwise extent of the computational domain is  $x/c \in [-2.4, 4]$  with the hump positioned from  $x/c = 0$  to 1, as illustrated in Figure 2. The vertical extent of the domain is  $y/c = 0.909$  with the top boundary lowered to contract the flow above the hump. This contraction is introduced to capture the effects of the side splitter plates [17]. The spanwise direction is taken to be periodic with an extent of  $z/c \in [0, 0.2]$ . The spatial domain is discretized with a structured grid with a near-wall grid resolution of  $\Delta x^+ = u_\tau \Delta x / \nu = 25$ ,  $\Delta y^+ = 0.25$ ,  $\Delta z^+ = 15$  around the hump. The overall grid size for the baseline (uncontrolled) simulation is  $48 \times 10^6$ .

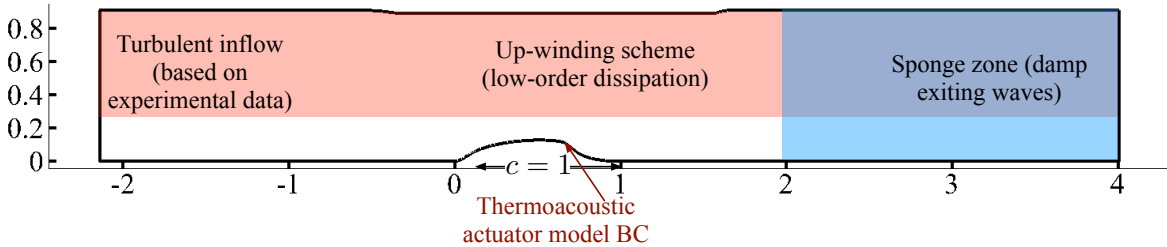


**Figure 2:** Geometry of the computational domain ( $xy$ -plane). The spanwise ( $z$ ) extent is 0.2 for three-dimensional computations. Turbulent inflow condition is specified at the inlet. Up-winding and the sponge zone are utilized to allow waves to leave the domain without numerical reflections.

This particular turbulent flow simulation is known to be sensitive to the upstream condition. The inlet boundary condition is set to match the experimental turbulent velocity profile reported in the workshop guidelines [17] and the experiments performed by Greenblatt *et al.* [24]. The inlet boundary layer profile is specified to match experimental measurement profile. We also ensure that the value of turbulent intensity is matched at the inlet to allow for turbulence to develop before reaching the leading edge of the hump. Turbulent fluctuation is added to the inlet profile with random Fourier modes [25, 26]. No-slip boundary condition is applied along the wall boundary. Along the outlet and the top of the boundary, we utilize the sponge zone to damp out any outgoing acoustic waves or exiting vortical

structures [27]. A first order up-winding scheme is applied away from the hump to damp out the exiting waves to ensure that waves do not artificially reflect back into the near field. The top boundary also utilizes the no-stress boundary condition.

### 3.1 Validation

To ensure that the present calculation accurately captures the flow physics, we compare the baseline separated flow over the hump with the experimental measurements of Seifert and Pack [18] ( $M_\infty = 0.25$ ,  $Re_\infty = 2.4$  to  $26 \times 10^6$ ), Greenblatt et al. [24] ( $M_\infty = 0.1$ ,  $Re_\infty = 1 \times 10^6$ ) and the numerical results of Franck and Colonius [20] ( $M_\infty = 0.25$ ,  $Re_\infty = 0.6 \times 10^6$ ). The present results are compared with the aforementioned results in Figures 3, 4, and 5. The pressure coefficient  $c_p \equiv (p - p_\infty)/(\frac{1}{2}\rho_\infty U_\infty^2)$  is compared in Figure 3. It can be observed that the present baseline result agrees very well with other experimental measurements throughout the domain. Our result also agrees reasonably well with numerical calculation by Franck and Colonius [20] but we note that the present study uses a larger grid size than theirs, which might have contributed to the slight difference.

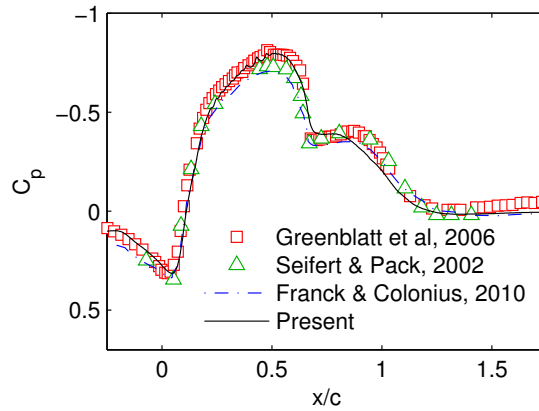


**Figure 3:** Comparison of pressure distribution over the hump.

The corresponding time-average velocity profiles are presented in Figures 4 and 5 and agree well with the PIV measurements of Greenblatt et al. [24] and computational findings of Franck and Colonius [20]. The Reynolds stress distribution is also found to match the experimental measurements. From these results, it has been observed that there are many common traits in the separated flow at these Reynolds numbers ( $Re_\infty = 0.5 \times 10^6$  and  $10^6$ ) and Mach numbers ( $M_\infty = 0.1$  and  $0.25$ ). There is some elongation of the recirculation region downstream of the hump for higher Mach number  $\approx 0.6$  as reported in Franck and Colonius [20].

For the chosen grid resolution and domain setup, the baseline results are found to be in agreement with those reported in past studies. The validated baseline simulation provides us with the test bed to explore the use of thermoacoustic flow control on the wall-mounted hump problem.

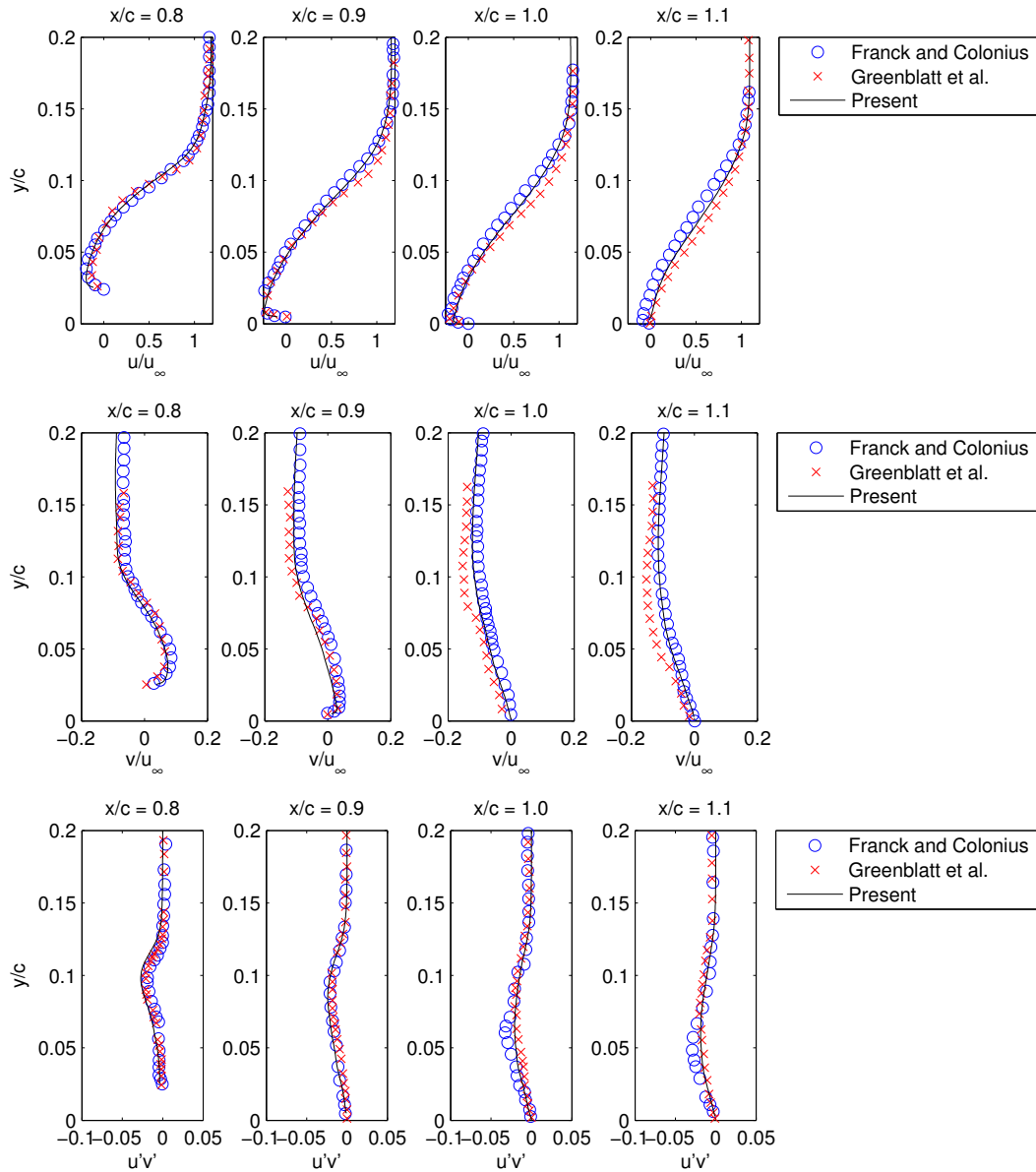


**Figure 4:** Comparison of time-average velocity and Reynolds stress for the baseline three-dimensional flow.

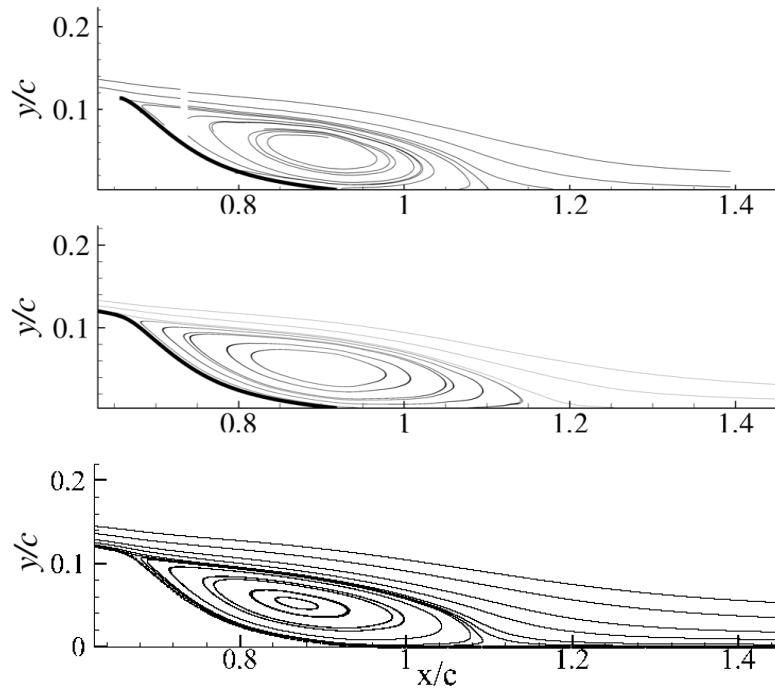


**Figure 5:** Comparison of the previous studies and the current study. From top to bottom: Greenblatt et al. [24] PIV,  $M = 0.1$ , and  $Re = 9.29 \times 10^5$ , Franck and Colonius [20] LES,  $M = 0.25$ , and  $Re = 5.0 \times 10^5$ , and the present LES study,  $M = 0.25$ , and  $Re = 5.0 \times 10^5$ .

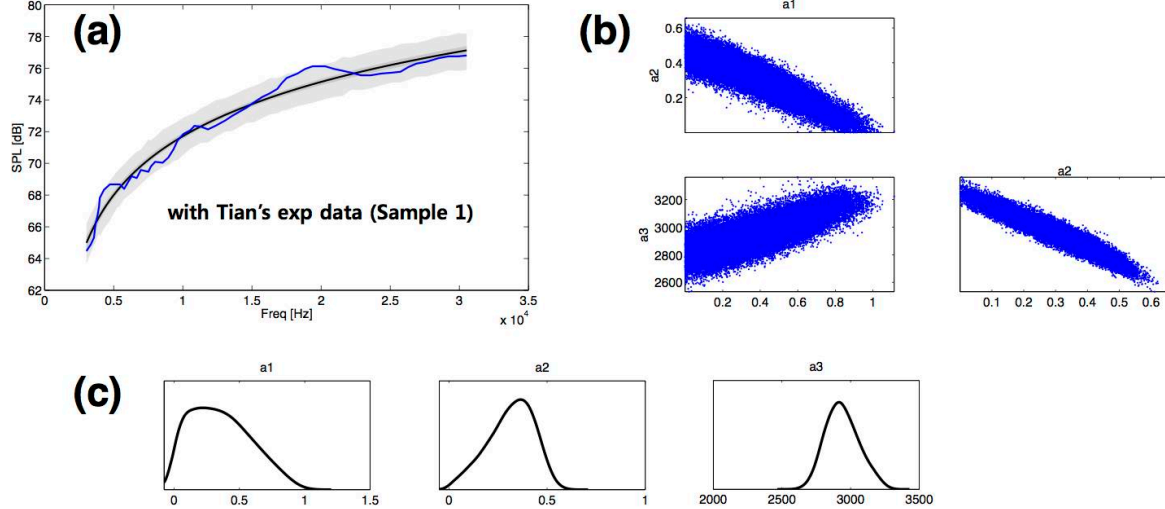


**Figure 6:** Uncertainty quantification of the model  $P = S(a_1T + a_2q + a_3 \frac{dT}{dt})$  and its (a) comparison with the experimental measurements of Tian et al. [6]. The shaded region constitutes the propagated uncertainty from the probability density profile. The correlations (b) between the coefficients and their probability distribution (c) are also revealed with MCMC.

## 4 Thermoacoustic Actuator Model

The generation of acoustic waves from graphene/carbon-nanotube based actuators is modeled by a thermal boundary condition in the present LES. In the early work of Arnold and Crandall [9], the input electrical power  $P$  is related to the temperature  $T$  of the actuator and its temporal derivative  $P = S(b_1T + b_2 \frac{dT}{dt})$ , where the coefficients are dependent on the material and configuration and  $S$  is the surface area of the actuator. The first term represents convective heat transfer and the second term captures the effect of capacitance. In addition to the above formulation, there are models [28] that include an extra heat flux term,  $P = S(a_1T + a_2q + a_3 \frac{dT}{dt})$ .

We have an ongoing theoretical and numerical investigation to quantify the significant of each term in the above model. The objective of this ongoing effort is to quantify the acoustic contribution from each term to accurately predict the performance of thermoacoustic actuators. This question is approached with the MCMC (Markov Chain Monte Carlo) method [29] to determine whether there is a correlation between the coefficients and how sensitive the choice of coefficients are since they do not appear to be directly measurable. Preliminary computations are shown in Figure 6 that compare the experimental measurement of Tian et al. [6] and the present MCMC results with uncertainty quantification.

For the purpose of the current flow control simulations, we have found that the use of sinusoidal heat flux  $q''_{\text{wall}} = \epsilon \cos(\omega t)$  (where  $\epsilon \ll 1$ ) to represent the actuator predicts the characteristics of the emitted acoustic waves reasonably well, as shown in Figure 7. A companion study [16] examining this actuator model has extended the acoustic piston model [30]. We have found that the thermal wavelength is very small compared to the acoustic

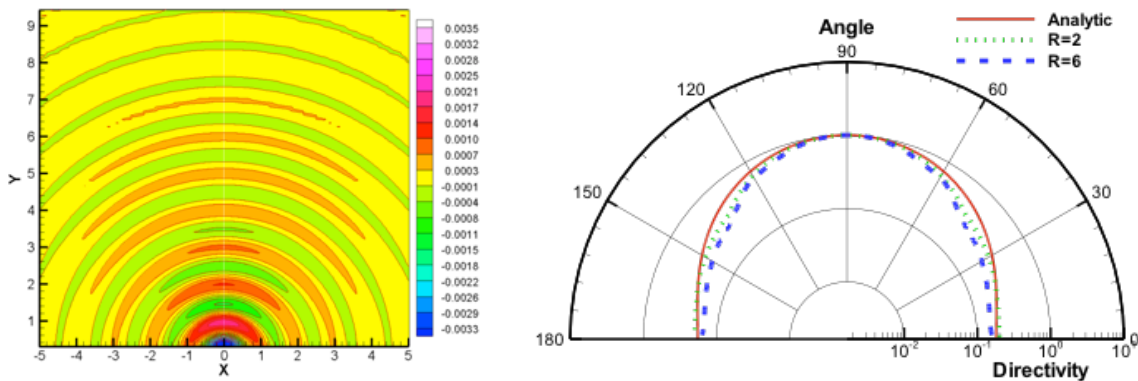


**Figure 7:** Simulated spherical thermoacoustic waves generated from a sinusoidal heat flux input on a flat plate. DNS results (left) and comparison of directivity with the FSU's analytical model (right).

wavelength and the thermal wave decays exponentially with the distance from the wall. We emphasize that the current flow control experiments are mainly concerned with how the acoustic waves interact with the turbulent separated flow and does not focus deeply into how the waves itself is created. Hence, we use the above heat flux boundary condition in the active flow control simulations shown below. We note that the ongoing study using MCMC will play an important role in determining the mechanism of how thermoacoustic actuators generate high-intensity waves and will guide the optimal design of these actuators down the road.

## 5 Active Flow Control with Acoustic Waves

In flow control simulations, we position the thermoacoustic actuator (boundary condition) near the separation point as a spanwise strip with a width  $\sigma$  of  $\sigma/c = 4.4 \times 10^{-3}$ . The width is selected to be the same as the width of the synthetic jet actuator slot used in the NASA validation study. The position of the actuator is also chosen to be at the same location, which is  $x/c = 0.6563$ . In future analysis, the importance of the actuator size and location will be examined. For the controlled cases, we must resolve the interaction between the high-frequency acoustic waves emitted by the actuator and the surrounding turbulent flow. This required us to further resolve the original grid and increased the overall grid size to be  $94.4 \times 10^6$  for the three-dimensional controlled case.

The primary frequency used in this study was based on a Helmholtz number ( $ka = 3$ ) [6]. For the experimental study the range of desirable frequencies for outputting high-intensity acoustic waves are above 10 kHz with the graphene-based actuator of size  $\approx 1\text{cm}$ . In this study, we normalize the frequency based on the width of the actuator ( $\mathcal{O}(10^{-3})$ ) such as  $f_a \equiv \hat{f}c/a_\infty = 107$ , where  $\hat{f}$  is the dimensional frequency. For the two-dimensional case, we also consider the higher harmonics of  $2f_0$  and  $10f_0$ .

The validity of the heat flux boundary condition is examined on the hump in a two-

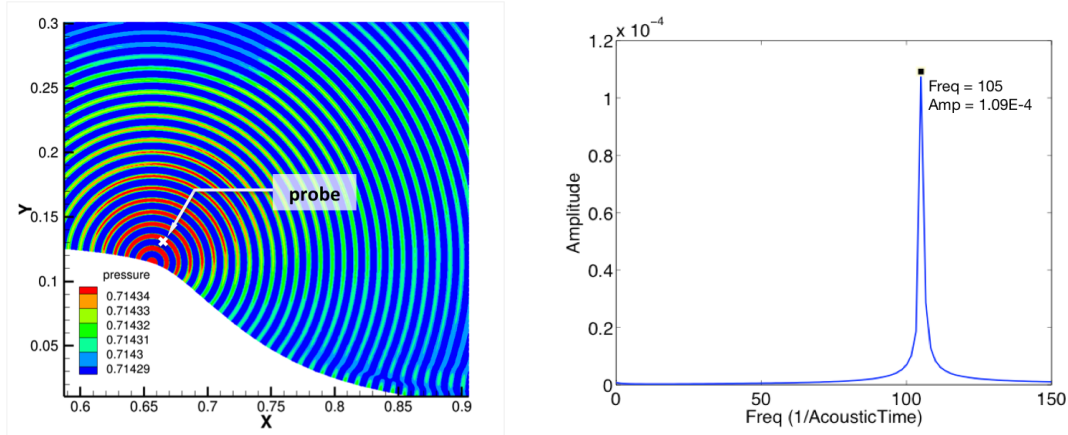


**Figure 8:** 2D simulated thermoacoustic waves generated from a sinusoidal heat flux input on the hump. LES pressure contour (left) and its spectrum at  $5w$  away from the actuator. SPL is 112 dB at this location.

dimensional domain with a quiescent condition using an actuation frequency of  $\omega = 2\pi f_a = 2\pi(107)$  and an amplitude of  $\epsilon_q = 0.00153$ , as shown in Figure 8 (left). The pressure is also monitored at the location  $5\sigma$  away normally from the hump surface and its spectrum is shown in Figure 8 (right). The measured SPL at this location is  $\approx 110$  dB, which is larger than  $\approx 85$  dB as reported by Tian et al. [6], who took measurements from a square area of actuator rather than a stripe arrangement. We use this large amplitude of 110dB to ensure we observe difference in the flow with control. Follow-up investigation will consider lower actuation amplitude and examine its influence on the control effectiveness. We note in passing that the drag and lift (coefficients) directly generated by actuation in quiescent flow are of order  $10^{-6}$ , which are practically negligible.

We present findings from the two and three-dimensional LES with thermoacoustic boundary condition applied for active flow control. Below we contrast the difference between the uncontrolled and controlled turbulent flow fields and discuss how the exerted aerodynamic force is altered. The three-dimensional LES requires significant amount of computational resource for the Reynolds number of  $0.5 \times 10^6$  since the grid sizes are large (48 and 94 million points for the baseline and controlled cases, respectively). While we are able to perform only a limited number of three-dimensional computations due to the large computational resource required, we have also conducted two-dimensional companion simulations to examine if acoustically controlled flow can alter the flow field with only two-dimensional instabilities. The acoustically controlled flow shows favorable results in reducing the drag on the wall-mounted hump for both two and three-dimensional cases.

## 5.1 Two-Dimensional Flow

First, we consider flow control with high-intensity acoustic waves for two-dimensional flow. The computational domain is chosen to be the same for three-dimensional simulations but with only a single cell in the spanwise direction (no spanwise variation). Simulations with three actuation frequencies of  $f_a = 107, 214, 1070$  are performed, in addition to the baseline.

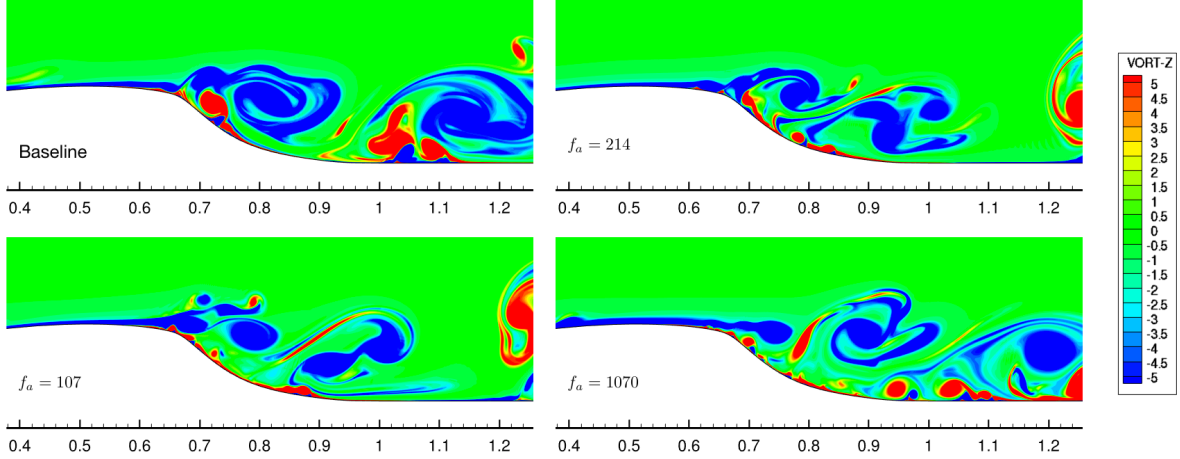


**Figure 9:** Instantaneous vorticity contour of the two-dimensional controlled flow for different actuation frequencies.

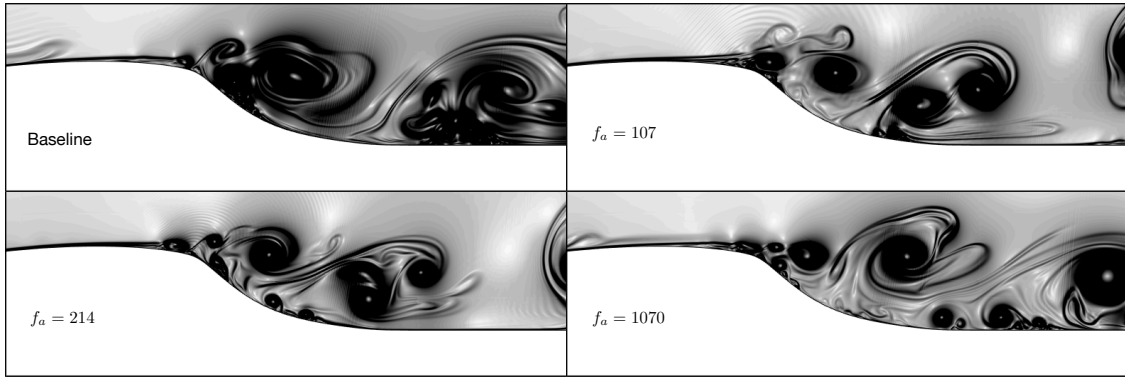


**Figure 10:** Numerical Schlieren of the two-dimensional controlled flow for different actuation frequencies.

The actuation frequency in terms of the Helmholtz number is approximately 3 for  $f_a = 107$ , which is based on the cutoff frequency achieved in the experimental settings of Tian et al. [6].

Due to the absence of spanwise variation, two-dimensional simulation reveals larger spanwise vortices forming and shedding from the wall-mounted hump. The spanwise vorticity contours are shown in Fig. 9 for both the uncontrolled and controlled cases. With high-frequency acoustic perturbations added, the spanwise vortices appear to become smaller compared to the baseline case, which is also evident from the Schlieren images in Fig. 10. In the Schlieren images, the emitted acoustic waves can be seen for  $f_a = 107$  and 214 while the waves become hardly visible in the figure for  $f_a = 1070$  for the highest actuation frequency. The acoustic perturbations appear to create small-scale structures that trigger the roll up of smaller vortices behind the hump. We also observe the generation of smaller opposite sign vortices near the wall.

The corresponding time-averaged vorticity plots are shown in Fig. 11, where we observe that spanwise vorticity is transported (convected) further downstream with actuation. We

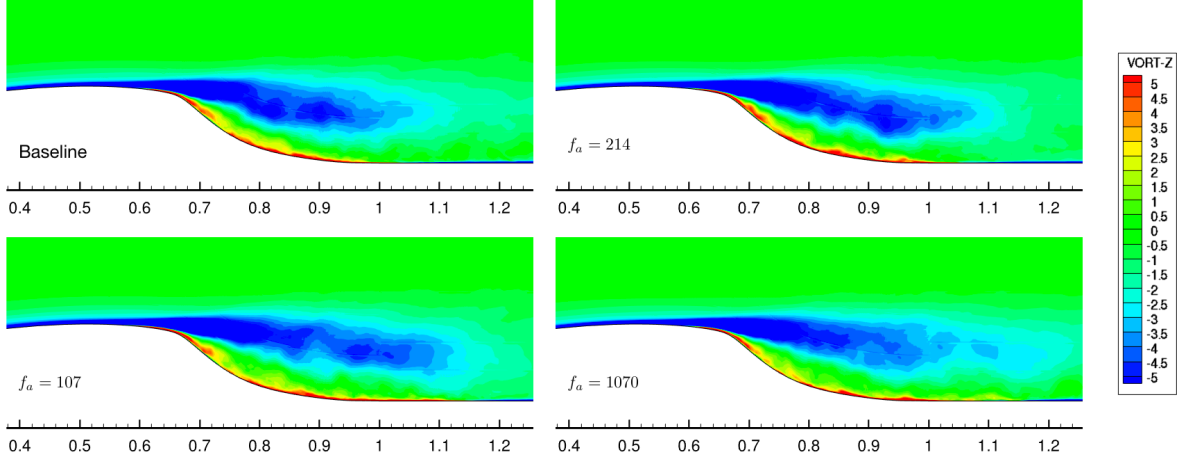


**Figure 11:** Time-average vorticity contour of the two-dimensional controlled flow for different actuation frequencies.

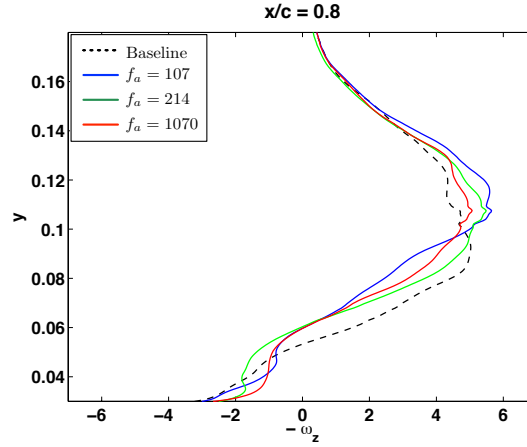


**Figure 12:** Slice of time-averaged spanwise vorticity ( $-\omega_z$ ) at  $x/c = 0.8$  for two-dimensional flow.

show in Fig. 12 the time-average vorticity profile at  $x/c = 0.8$  to illustrate that the vortex sheet emanating from the separation point becomes thinner with control. This allows for the sheet to convect downstream with delayed growth of large-scale instability and the circulation zone to elongate in the streamwise direction, as presented in Fig. 13. Also shown in the same figure are the pressure contours. The low-pressure zone behind the hump moves backward and the recirculation region elongates, in particular for the controlled cases of  $f_a = 107$  and  $f_a = 1070$ .

The elongation of the recirculation region correlates to the cases with the largest reduction in drag, as seen in Table 1. Since the low-pressure core is pushed further downstream, the drag force on the hump is decreased. The pressure coefficient over the hump is plotted in Figure 14. We note that upstream of the separation point there appears to be only minor differences between the baseline and the actuation cases. This tells us that the drag reduction

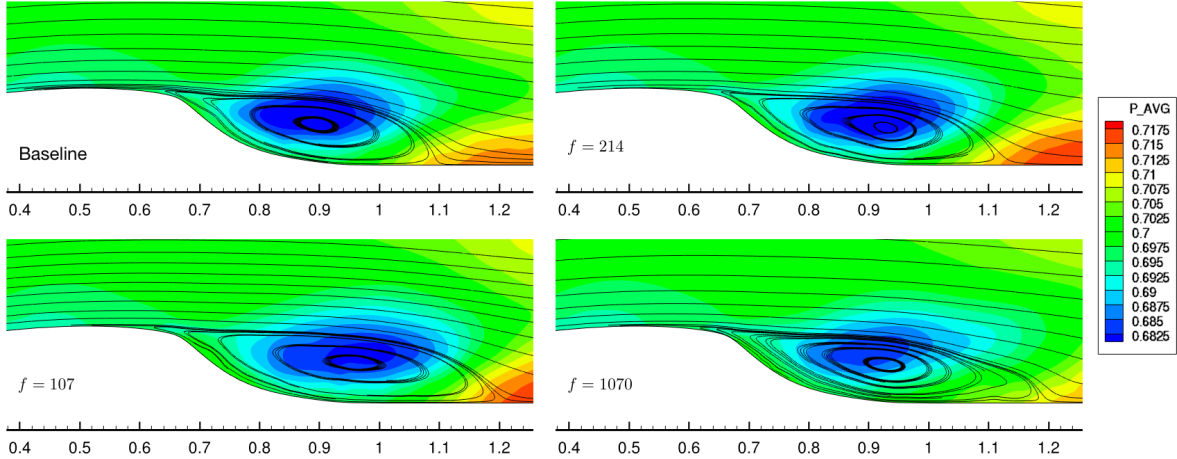


**Figure 13:** Time-average streamlines and pressure for the two-dimensional controlled flow for different actuation frequencies.

Cases	$C_D$ ( $10^{-2}$ )	$\Delta C_D$
Baseline	5.56	--
$f_a = 107$	5.01	-9.9%
$f_a = 214$	5.51	-0.9%
$f_a = 1070$	4.93	-11.4%

**Table 1:** Drag reduction with acoustic flow control for two-dimensional flow.

comes from the modifications made in the wake. The acoustic flow control is able to reduce the drag on the hump by up to 11.4% for two-dimensional flow. The wake elongation used for drag reduction is of an opposite trend from how synthetic jet controls the flow over the hump in past studies. With synthetic jets, recirculation zones are reduced in size for recovering pressure losses to achieve drag reduction.

Spectrum of lift is also shown in Figure 15, where the decrease of dominant peak amplitudes for the controlled case is observed. The actuation frequencies are also marked (see logarithmic plot on right) and can be seen to be of very limited spectral power. The use of acoustic perturbation does not ‘directly’ shift the flow, but appears to trigger instability differently to the controlled flow that alters the global flow field. This approach shares similarity with the flow control on a jet using high-frequency piezoelectric actuator performed by Wiltse and Glezer [11].

## 5.2 Three-Dimensional Flow

Next, we consider the effect of high-intensity acoustic waves on three-dimensional turbulent flow over the hump. Due to the large computational time required to perform the LES calculation on the DoD cluster, we have limited our controlled simulation to be for a single case with  $f_a = 107$  and amplitude of 110dB (SPL).

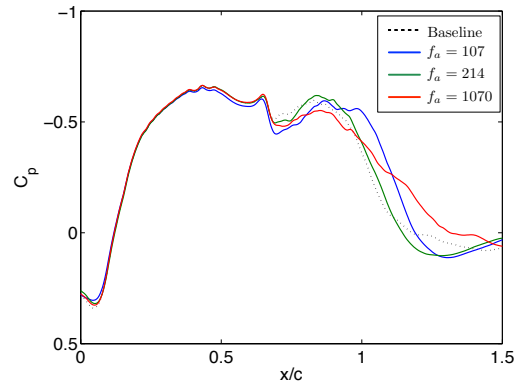


**Figure 14:** Time-averaged pressure coefficient over the hump for two-dimensional controlled flow.

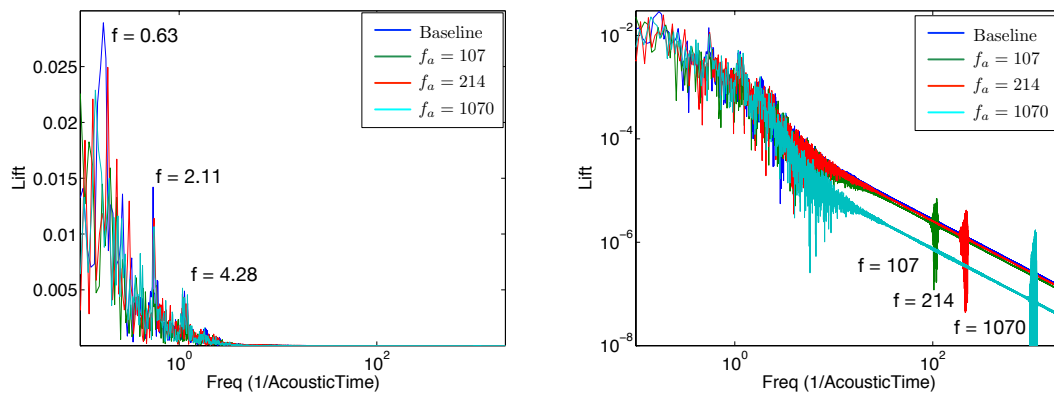


**Figure 15:** Lift spectra with flow control of two-dimensional flow presented on linear and logarithmic scales.

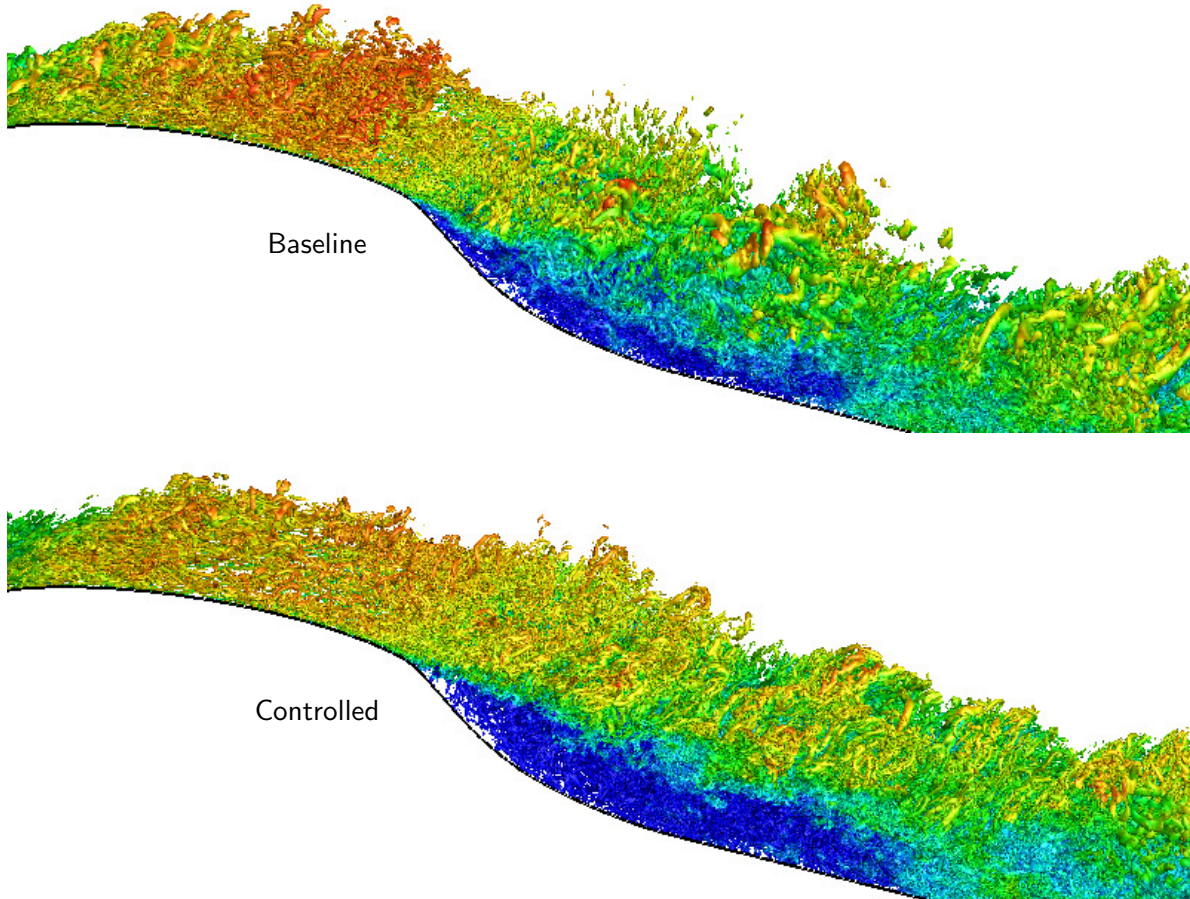


**Figure 16:** Comparison of the baseline and acoustically controlled ( $f_a = 107$ ) instantaneous flow fields downstream of the wall-mounted hump. Three-dimensional structures are visualized by the  $Q$ -criterion colored with streamwise velocity. Note that the turbulent structures are smaller with elongated wake for the controlled flow using high-intensity acoustic waves.

The instantaneous three-dimensional flow fields from the baseline and controlled cases are shown in Fig. 16. The controlled simulation required a finer grid resolution around the actuator location to resolve the interaction between the acoustic waves and the turbulent structures. The overall grid size for the controlled flow is 94 million points. We believe both the uncontrolled and controlled cases are resolved well since the baseline case has been well validated as discussed earlier and the vortical wake structures for the controlled flow are well-captured as it can be seen in the numerical Schlieren in Fig. 17. We notice that the turbulence flow structures become finer and the wake is elongated with acoustic control. These observations are aligned with those made for two-dimensional flow discussed above. The three-dimensional vortical structures are of course much finer due to the variations allowed in the spanwise direction.

In Fig. 16, the large blue region (low velocity region) is prominent in the controlled case and is obvious that separated region extends further downstream of the hump. This growth

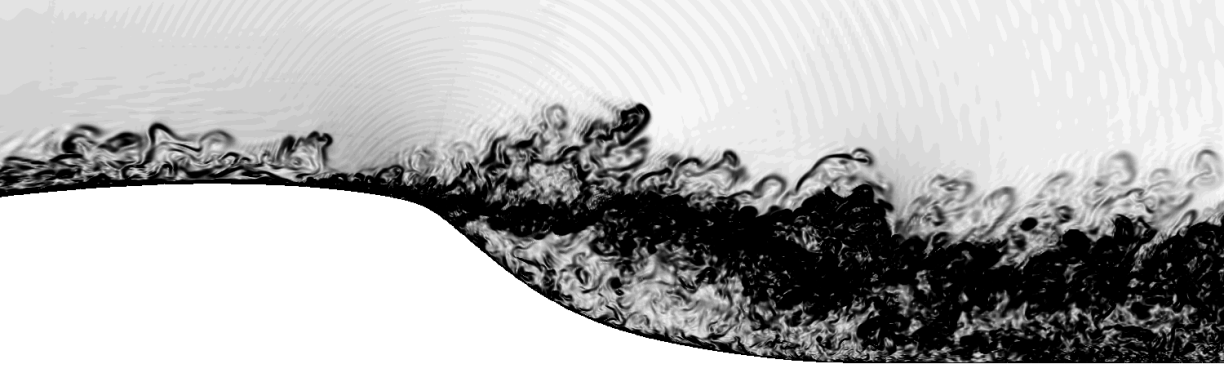


**Figure 17:** Numerical Schlieren of the three-dimensional controlled flow with an actuation frequency of  $f_a = 107$ .

for three-dimensional flow can be seen clearly from Fig. 18. The recirculation zone for the controlled case is found to elongate by approximately 15% compared to the baseline case. This elongation also shifts downstream the low-pressure region associated with the wake and leads to drag reduction as compared in Table 2.

Cases	$C_d (10^{-2})$	$\Delta C_D$
Baseline	3.31	--
$f_a = 107$	3.12	-5.8%

**Table 2:** Drag reduction with acoustic flow control for three-dimensional flow.

Let us further analyze the shear layer with the time-average profile of spanwise vorticity using Figs. 19 and 20. It can be noted that the vortex sheet is thinner and convects further downstream with the use of actuation. The comparison of the vorticity distribution shows less spreading of vorticity for the controlled flow in Fig. 20. Thinning of the vorticity profile at this location supports the argument that the sheet needs to advect further downstream to spread and reattach to the wall, which in turn elongates the recirculation zone. Since the vorticity profile upstream of the separation point cannot change much, the control effort with acoustics is aimed at modifying the spreading rate of spanwise vorticity to change the wake profile.

The addition of the high-frequency pressure oscillations to the flow creates small-scale structures. These small-scale structures appear to suppress the production of large vortices that exist in the uncontrolled flow. The instantaneous pressure and vorticity contours in Fig. 21 illustrate this observation. In fact, the turbulent energy in the shear layer appears to decrease with control as shown by the reduction of Reynolds stress in Fig. 22. From this figure, we see that the magnitude of fluctuations in the shear layer decrease with the added acoustic waves. For the unactuated case, the inherent shear layer instability and the vortex sheet roll up cause large-scale fluctuation in the wake. Conversely, for the actuated case the fluctuations near the separation point are decreased and the shear layer breaks down

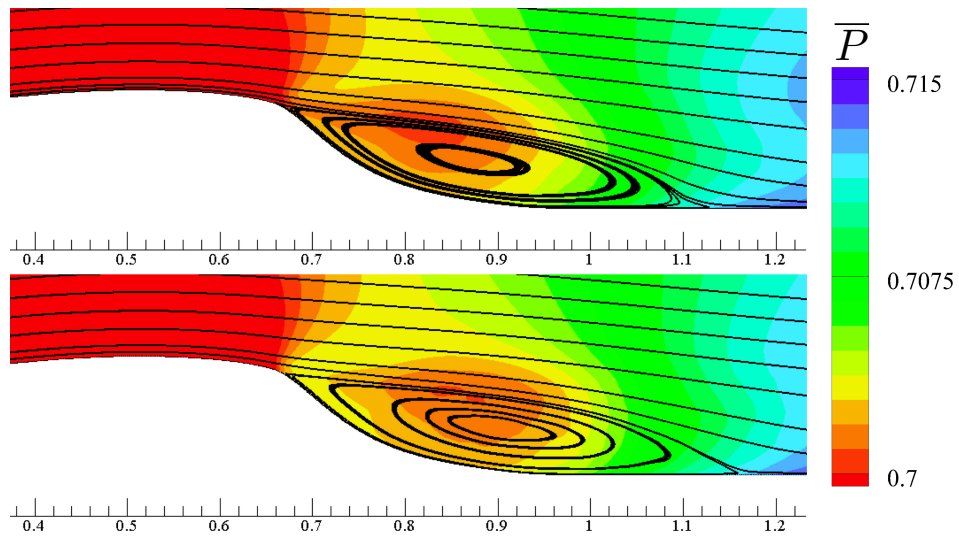


**Figure 18:** Time-averaged streamlines for baseline (top) and the actuated case (bottom) for three-dimensional flow.

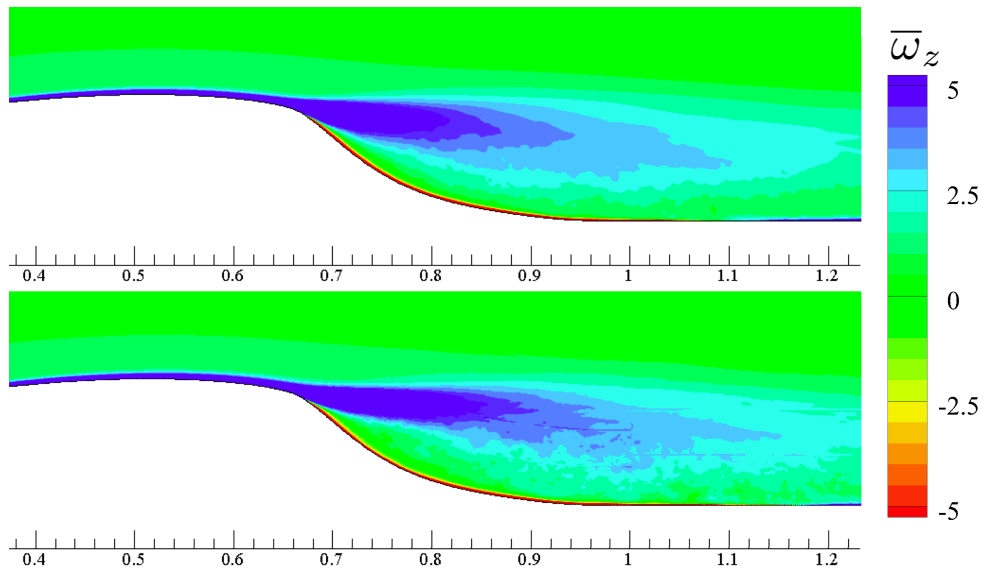


**Figure 19:** Time-averaged spanwise vorticity ( $\omega_z$ ) for baseline (top) and actuated (bottom) three-dimensional flow.

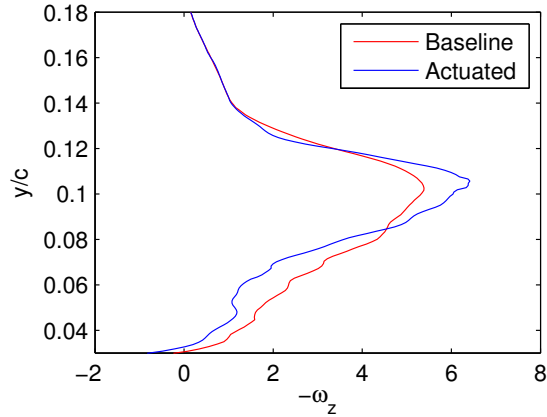


**Figure 20:** Slice of time-averaged spanwise vorticity ( $\omega_z$ ) for three-dimensional flow at  $x/c = 0.8$ .

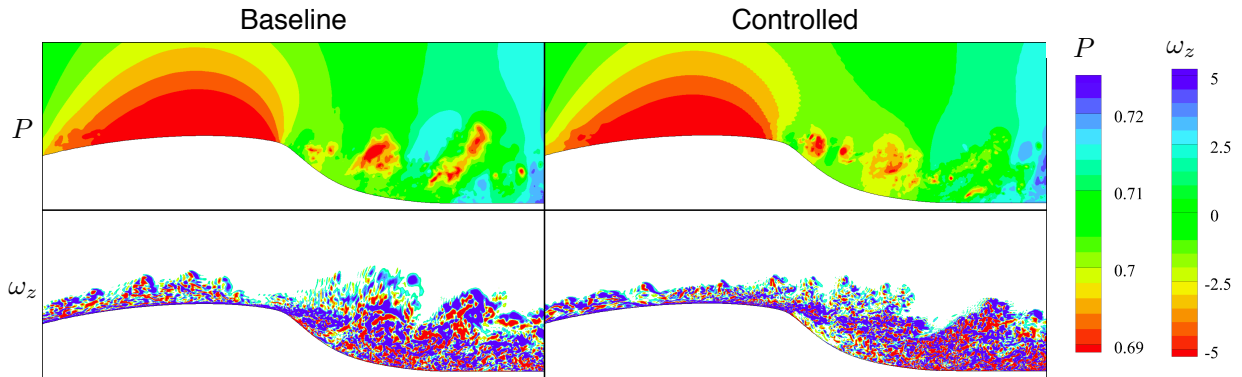


**Figure 21:** Instantaneous three-dimensional flow field images for the baseline and actuated cases. Pressure contours on the top and spanwise vorticity contours on the bottom.

further downstream. It appears that the interaction of the high-intensity acoustic waves and the shear layer instability plays a large role in how small-scale spanwise vortices develop and affect the formation of larger-scale vortical structures. The reduction in the size of the vortex sheet roll-up appears to result in elongating the recirculation zone. Furthermore, the observations made for three-dimensional flows are in agreement with two-dimensional flows. This suggests that the main mechanism for acoustic control with the current actuator setup is two-dimensional in nature.

## 6 Summary

In this investigation, we have numerically examined the use of high-intensity acoustic waves for the control of separated flow over a wall-mounted hump. The computations were performed for a chord-based Reynolds number of  $0.5 \times 10^6$  and Mach number of 0.25 using large-eddy simulations. The uncontrolled baseline calculation was validated with experi-

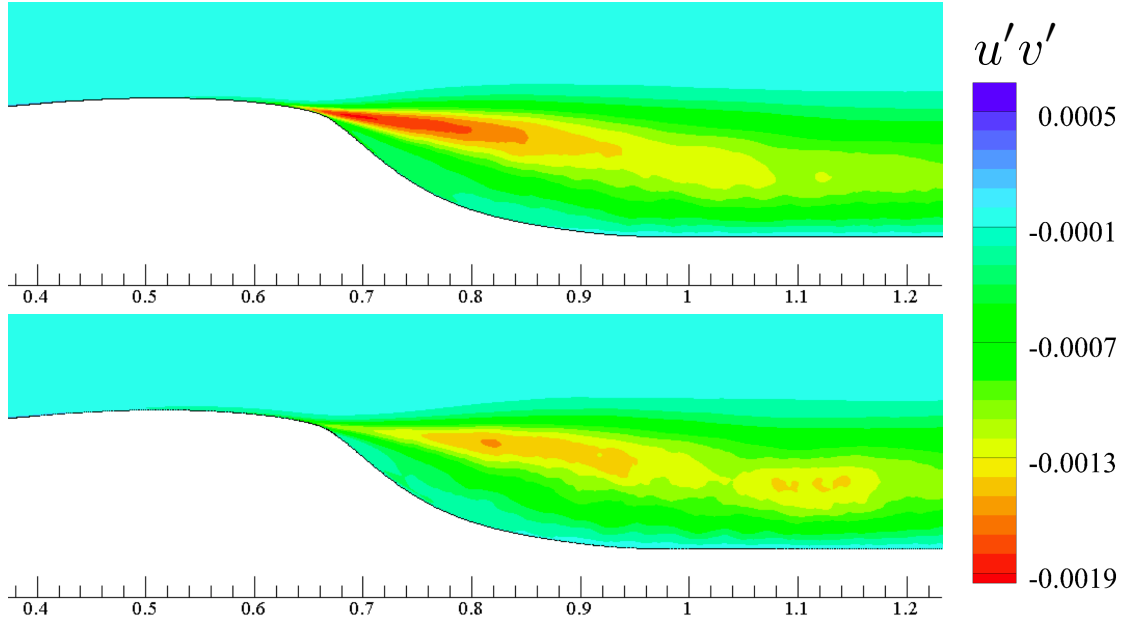


**Figure 22:** Reynolds stress at the rear of the hump for three-dimensional flow. Shown are the baseline (top) and actuated cases (bottom).

mental and computational results available in the literature and was observed to be in good agreement. In order to accurately predict the baseline turbulent flow field, a grid size of 48 million was required, which called for the use of a large-size computer cluster made available through the HPCMP program at the Department of Defense.

The generation of thermoacoustic waves was analyzed to determine an appropriate boundary condition for LES. A sinusoidal heat flux condition was found to be sufficient in the present study to be utilized as a wall boundary condition to create acoustic waves having sound pressure level of 110dB, measured five slot widths away from the actuator, in quiescent flow around the hump geometry. This particular boundary condition was then used for the control of two and three-dimensional turbulent flow over the hump. The actuation frequency for these cases were chosen based on the physical limitation of the graphene-based thermoacoustic actuator, which is Helmholtz number  $ka \approx 3$ .

It was observed that high-intensity high-frequency actuation modifies the global behavior of the two and three-dimensional flow over the hump to achieve drag reduction. In both flows, the recirculation zone downstream of the hump was elongated in the streamwise direction. The emitted acoustic waves introduced pressure perturbations to the separated flow that suppressed the formation of large-scale shedding vortices by triggering the formation of smaller-scale vortices, thus allowing for the shear layer to stably convect further downstream. This resulted in the controlled wake having an elongated recirculation zone with the associated low-pressure region shifted downstream leading to reduced drag on the hump. We noted that this control mechanism is different from those used by synthetic jets or plasma actuators, which enhance mixing between the high and low-momentum fluids to reduce the

size of the recirculation zone for lower drag. The present acoustic control achieved approximately 10% and 6% of drag reduction for two and three-dimensional flow, respectively, with 110dB of actuator input.

The results from this 9-month STIR effort appear promising to aid the development of thermoacoustic actuator that can be locally mounted on a surface of arbitrary geometry. The added attractiveness of this actuator is the reduced power input to deliver the high-intensity waves as the output. The required power input is inversely proportional to the material heat capacity, which is extremely low for carbon-based materials (e.g., graphene or carbon nanotube based membranes). To gain further understanding of the physics behind how locally introduced high-intensity acoustic waves can be used for modifying the behavior of turbulence, additional large-scale simulations and stability analysis should be performed. It would also be essential to conduct some parametric analysis to examine the influence of sound pressure level and actuator frequency to design effective and efficient acoustic flow control strategy. The results reported here should be able to serve as a basis to advance thermoacoustic actuator and flow control technologies.

## 7 Personnel

The following members at the Florida State University were involved in this STIR research effort.

Faculty:	Prof. Kunihiro Taira Prof. William Oates
Postdoctoral Associate:	Dr. Jonghoon Bin*
Graduate Students:	Phillip Munday* Chi-An Yeh* Ryan Jantzen*

\*partially supported by the present grant.

## Acknowledgments

This research was supported by the U.S. Army Research Office (Award Number W911NF-13-1-0062, Program Manager: Dr. Frederick Ferguson). The discussions on thermoacoustic actuators and flow control with Dr. Bryan Glaz and Dr. Matthew Munson at Aberdeen Proving Ground (ARL) are gratefully acknowledged. The computations were performed on the large-scale cluster made available through the High Performance Computing Modernization Program at the Department of Defense.

## References

- [1] Joslin, R. D. and Miller, D. N., editors, *Fundamentals and applications of modern flow control*, AIAA, 2009.
- [2] Cattafesta, L. N. and Sheplak, M., “Actuators for active flow control,” *Annu. Rev. Fluid Mech.*, Vol. 43, 2011, pp. 247–272.
- [3] Glezer, A. and Amitay, M., “Synthetic jets,” *Annu. Rev. Fluid Mech.*, Vol. 34, 2002, pp. 503–529.
- [4] Corke, T. C., Enloe, C. L., and Wilkinson, S. P., “Dielectric barrier discharge plasma actuators for flow control,” *Annu. Rev. Fluid Mech.*, Vol. 42, 2010, pp. 505–529.
- [5] Crittenden, T. M. and Raghu, S., “Combustion powered actuator with integrated high frequency oscillator,” *Int. J. Flow Control*, Vol. 1, 2009, pp. 87–97.
- [6] Tian, H., Ren, T.-L., Xie, D., Wang, Y.-F., Zhou, C.-J., Feng, T.-T., Fu, D., Yang, Y., Peng, P.-G., Wang, L.-G., and Liu, L.-T., “Graphene-on-Paper Sound Source Devices,” *ACS Nano*, Vol. 5, No. 6, 2011, pp. 4878–4885.
- [7] Hu, H., Zhu, T., and Xu, J., “Model for thermoacoustic emission from solids,” *App. Phys. Lett.*, Vol. 96, 2010, pp. 214101.
- [8] Baloch, K. H., Voskanyan, N., Bronsgeest, M., and Cumings, J., “Remote joule heating by a carbon nanotube,” *Nature Nanotechnology*, Vol. 7, May 2012, pp. 316–319.
- [9] Arnold, H. D. and Crandall, I. B., “The Thermophone as a Precision Source of Sound,” *Phys. Rev. B*, Vol. 10, 1917, pp. 22–38.
- [10] Xiao, L., Chen, Z., Feng, C., Liu, L., Bai, Z.-Q., Wang, Y., Qian, L., Zhang, Y., Li, Q., Jiang, K., and Fan, S., “Flexible, stretchable, transparent carbon nanotube thin film loudspeakers,” *Nano Letters*, Vol. 8, No. 12, 2008, pp. 4539–4545.
- [11] Wiltse, J. M. and Glezer, A., “Direct excitation of small-scale motions in free shear flows,” *Phys. Fluids*, Vol. 10, No. 8, 1998, pp. 2026–2036.
- [12] Rockwell, D. and Knisely, C., “The organized nature of flow impingement upon a corner,” *J. Fluid Mech.*, Vol. 93, No. 3, 1979, pp. 413–432.
- [13] Tam, C. K. W. and Ahuja, K. K., “Theoretical model of discrete tone generation by impinging jets,” *J. Fluid Mech.*, Vol. 214, 1990, pp. 67–87.
- [14] Zaman, K. B. M. Q., Bar-Sever, A., and Mangalam, S. M., “Effect of acoustic excitation on the flow over a low-Re airfoil,” *J. Fluid Mech.*, Vol. 182, 1987, pp. 127–148.
- [15] Lang, W., Poinot, T., and Candel, S., “Active control of combustion instability,” *Comb. Flames*, Vol. 70, No. 3, 1987, pp. 281–289.

- [16] Bin, J., Oates, W. B., and Taira, K., “Thermoacoustic wave generation model for graphene based membrane,” 2013 in preparation.
- [17] Sellers, W. L. and Rumsey, C. L., “Langley Research Center Workshop: CFD Validation of Synthetic Jets and Turbulent Separation Control, 2004,” .
- [18] Seifert, A. and Pack, L. G., “Active Flow Separation Control on Wall-Mounted Hump at High Reynolds Numbers,” *AIAA J.*, Vol. 40, No. 7, 2002, pp. 1363–1372.
- [19] Rumsey, C. L., “Proceedings of the 2004 Workshop on CFD Validation of Synthetic Jets and Turbulent Separation Control,” Tech. Rep. NASA/CP-2007-214874, NASA, 2007.
- [20] Franck, J. A. and Colonius, T., “Compressible Large-Eddy Simulation of Separation Control on a Wall-Mounted Hump,” *AIAA J.*, Vol. 48, No. 6, 2010, pp. 1098–1107.
- [21] Khalighi, Y., Nichols, J. W., Ham, F., Lele, S. K., and Moin, P., “Unstructured Large Eddy Simulation for Prediction of Noise Issued from Turbulent Jets in Various Configurations,” 17th AIAA/CEAS Aeroacoustics Conference, 2011.
- [22] Khalighi, Y., Ham, F., Moin, P., Lele, S., Schlinker, R., Reba, R., and J., S., “Noise Prediction of Pressure-Mismatched Jets Using Unstructured Large Eddy Simulation,” Proceedings of ASME Turbo Expo, Vancouver, 2011.
- [23] Brés, G. A., Nichols, J. W., Lele, S., and Ham, F. E., “Towards Best Practices for Jet Noise Predictions with Unstructured Large Eddy Simulations,” 42nd AIAA Fluid Dynamics Conference, New Orleans, 2012.
- [24] Greenblatt, D., Paschal, K. B., Yao, C.-S., Harris, J., Schaeffer, N. W., and Washburn, A. E., “Experimental investigation of separation control. Part 1: baseline and steady suction,” *AIAA J.*, Vol. 44, No. 12, 2006, pp. 2820–2830.
- [25] Béchara, W., Bailly, C., Lafon, P., and Candel, S. M., “Stochastic approach to noise modeling for free turbulent flows,” *AIAA J.*, Vol. 32, No. 3, 1994, pp. 455–463.
- [26] Franck, J. A., *Large-Eddy simulation of flow separation and control on a wall-mounted hump*, Ph.D. thesis, California Institute of Technology, 2009.
- [27] Freund, J. B., “Proposed inflow/outflow boundary condition for direct computation of aerodynamic sound,” *AIAA J.*, Vol. 35, No. 4, 1997, pp. 740–742.
- [28] Lim, C. W., Tong, L. H., and Li, Y. C., “Theory of suspended carbon nanotube thinfilm as a thermo-acoustic source,” *J. Sound Vib.*, Vol. 332, 2013, pp. 5451–5461.
- [29] Haario, H., Saksman, E., and Tamminen, J., “An adaptive metropolis algorithm,” *Bernoulli*, Vol. 7, No. 2, 2001, pp. 223–242.
- [30] Blackstock, D. T., *Fundamentals of physical acoustics*, Wiley-Interscience, 2000.